X-RAY EMISSION AND CORONA OF THE YOUNG INTERMEDIATE-MASS BINARY theta(1) Ori E

The Astrophysical Journal, 707:942–953, 2009 December 20 doi:10.1088/0004-637X/707/2/942

X-RAY EMISSION AND CORONA OF THE YOUNG INTERMEDIATE-MASS BINARY θ^1 Ori E

David P. Huenemoerder[1], Norbert S. Schulz[1], Paola Testa[2], Anthony Kesich[1], and Claude R. Canizares[1]
[1] Massachusetts Institute of Technology, Kavli Institute for Astrophysics and Space Research, 70 Vassar St., Cambridge, MA 02139, USA
[2] Harvard-Smithsonian Center for Astrophysics, 60 Garden St., Cambridge, MA 02138, USA
Received 2009 August 6; accepted 2009 October 29; published 2009 November 30

ABSTRACT

θ^1 Ori E is a young, moderate mass binary system, a rarely observed case of spectral-type G-giants of about 3 solar masses, which are still collapsing toward the main sequence, where they presumably become X-ray faint. We have obtained high-resolution X-ray spectra with *Chandra* and find that the system is very active and similar to coronal sources, having emission typical of magnetically confined plasma. It has a broad temperature distribution with a hot component and significant high energy continuum; narrow emission lines from H- and He-like ions, as well as a range of Fe ions, and relative luminosity, $L_x/L_{\rm bol} = 10^{-3}$, at the saturation limit. Density, while poorly constrained, is consistent with the low density limits, our upper limits being $n_e < 10^{13}$ cm^{-3} for Mg XI and $n_e < 10^{12}$ cm^{-3} for Ne IX. Coronal elemental abundances are sub-solar, with Ne being the highest at about 0.4 times solar. We find a possible trend in Trapezium hot plasmas toward low relative abundances of Fe, O, and Ne, which is hard to explain in terms of the dust depletion scenarios of low-mass young stars. Variability was unusually low during our observations relative to other coronally active stars. Qualitatively, the emission is similar to post-main-sequence G-stars. Coronal structures could be compact or comparable to the dimensions of the stellar radii. From comparison to X-ray emission from similar mass stars at various evolutionary epochs, we conclude that the X-rays in θ^1 Ori E are generated by a convective dynamo, present during contraction, but which will vanish during the main-sequence epoch possibly to be resurrected during post-main-sequence evolution.

Key words: stars: coronae – stars: individual (tet01 Ori E) – stars: pre-main sequence – X-rays: stars

1. INTRODUCTION

Intermediate-mass pre-main-sequence (PMS) stars, like their massive cousins, are difficult to study because of their rapid evolutionary timescales. Though not as short as stars above 8 $M_\odot$ which take less than 10^5 years to reach the main sequence, intermediate-mass stars between 2 $M_\odot$ and 8 $M_\odot$ may only take 10–20 Myr. In both cases, the accretion timescales dominate the evolution time to the zero-age main sequence (ZAMS), in contrast to the low-mass T Tauri stars for which PMS contraction times are longest. Intermediate-mass PMS stars are also not easily found and identified, and most existing studies focus on Herbig Ae and Be (HAeBe) stars. Herbig stars (Herbig 1960) are recognized as such once they have already contracted to high enough photospheric temperatures to be optically identified as A and B stars and are thus already close to the ZAMS. Herbig stars mark the transition between formation mechanisms of low-mass and high-mass stars (Baines et al. 2006). Herbig Ae stars seem more similar to low-mass T Tauri stars (Waters & Waelkens 1998; Vink et al. 2005). Herbig Be stars are more similar to embedded young massive stars (Drew et al. 1997). Both Ae and Be stars are all already in fairly late PMS stages.

Most studies of Herbig stars use infrared and optical wavelengths to probe their circumstellar disks and dusty environments. Recent studies suggest that specifically in HAe stars there is evidence not only for circumstellar disks (Mannings & Sargent 1997; Grady et al. 1999) but also indications of dust shadowing and settling indicative of dust grain growth and planetesimal formation (Acke & Waelkens 2004; Dullemond & Dominik 2004; Grady et al. 2005). Some studies also suggest that magnetospheric accretion analogous to classical T Tauri stars is possible (Muzerolle et al. 2004; Grady et al. 2004; Guimarães et al. 2006). Recent modeling of 37 Herbig Ae/Fe stars using UV spectra revealed that all but one show indications of accretion with accretion rates in many cases substantially exceeding 10^{-8} $M_\odot$ yr^{-1} (Blondel & Djie 2006).

Binarity also seems to be an important attribute in the formation and evolution of intermediate-mass stars. In a sample of 28 HAeBe stars, Baines et al. (2006) find a binarity fraction of almost 70% with a higher binary frequency in HBe stars than in HAe stars. HAe stars with close companions also seem to lack circumstellar disks (Grady et al. 2005).

X-ray studies of young intermediate-mass stars are still quite rare and to date also focus almost entirely on HAe stars. Systematic studies have shown that these are moderately bright in X-rays (Damiani et al. 1994; Zinnecker & Preibisch 1994; Hamaguchi et al. 2005; Stelzer et al. 2006b). This fact is already quite remarkable since main-sequence A stars lack strong winds or coronae and it suggests that the physical characteristics of HAe stars differ from those of main-sequence A- and B stars. Mechanisms suggested range from active accretion to coronal activity to some other form of plasma confinement. It is also possible, given the high frequency of binaries among HAeBe stars, that some X-ray sources could be due to late-type companions (Stelzer et al. 2006a, 2006b). A detailed summary can be found in a recent *Chandra* high-resolution spectroscopic study of the HAe star HD 104237 in the ϵ Chamaeleontis Group (Testa et al. 2008).

In this paper, we focus on X-ray emission from θ^1 Ori E, which was recently determined to be an intermediate-mass binary star. The Orion Trapezium is generally known for its ensemble of the nearest and youngest massive stars (Schulz et al. 2001, 2003; Stelzer et al. 2005). Recent studies now suggest the presence of several intermediate-mass stars. θ^2 Ori A harbors the second most massive O-star of the Trapezium, but also two unidentified intermediate-mass stars both between 3 $M_\odot$ and 7 $M_\odot$ (Preibisch et al. 1999). The system is particularly interesting in X-rays for its high luminosity and hard spectral

Table 1
Observation Log

N[a]	Date	Time	t_{exp} (ks)	ϕ[b]	C[c]	Rate$\times 10^3$ (counts s^{-1})	Flux[d]$\times 10^3$ (phot cm^{-2} s^{-1})	Flux[d]$\times 10^{12}$ (ergs cm^{-2} s^{-1})	v[e] (km s^{-1})
3	1999 Oct 31	05:47:21	49	0.55	...	105	1.105 (0.033)	3.30 (0.10)	−11 (22)
4	1999 Nov 24	05:37:54	31	0.93	H	83	1.250 (0.025)	3.55 (0.07)	−6 (52)
2567	2001 Dec 28	12:25:56	46	0.30	...	69	0.873 (0.033)	2.27 (0.09)	65 (55)
2568	2002 Feb 19	20:29:42	46	0.70	HM	...	...	...	...
7407	2006 Dec 03	19:07:48	25	0.33	...	88	1.085 (0.052)	3.17 (0.15)	68 (49)
7410	2006 Dec 06	12:11:37	13	0.60	...	77	1.030 (0.072)	2.87 (0.20)	−4 (72)
7408	2006 Dec 19	14:17:30	25	0.93	...	78	0.994 (0.049)	2.88 (0.14)	−35 (60)
7409	2006 Dec 23	00:47:40	27	0.28	...	90	1.140 (0.050)	3.43 (0.15)	96 (40)
8897	2007 Nov 15	10:03:16	24	0.35	...	84	1.065 (0.052)	3.16 (0.15)	72 (41)
8896	2007 Nov 30	21:58:33	23	0.93	M	25	1.030 (0.043)	3.00 (0.13)	−7 (82)
8895	2007 Dec 07	03:14:07	25	0.55	...	86	1.045 (0.049)	3.10 (0.15)	86 (37)

Notes.
[a] N is the *Chandra* observation identifier number.
[b] Orbital phase (ϕ) was computed from the ephemeris of Herbig & Griffin (2006).
[c] The "C" column indicates spectra with severe confusion; "H" and "M" respectively indicate whether the HEG or MEG spectrum could not be used.
[d] The model-independent average flux in the 2–17Å range, computed from HEG and MEG counts, flux corrected using the responses.
[e] The line-of-sight velocity, heliocentric correction applied. Values in parentheses are the 90% error bar ($\sim 1.6\sigma$). See Section 2.4.1 for explanation.

properties as well as giant hard X-ray outbursts (Feigelson et al. 2002; Schulz et al. 2006). Plasma temperatures during these outbursts exceed 10^8 K (Schulz et al. 2006). While the latter authors suggested a possible link of these outbursts to binary interactions involving the closer intermediate-mass companion, there is also some evidence that these may be connected to the more distant companion (M. Gagne 2008, private communication).

θ^1 Ori E is another system now known to contain young intermediate-mass stars. It was long misidentified as B5–B8 spectral type (Parenago 1954; Herbig 1960). Herbig & Griffin (2006) obtained optical spectroscopic radial velocity measurements and identified the system as a binary containing two G III type stars of masses of about 3–4 $M_\odot$ in a 9.9 day orbit. Evolutionary tracks constrain the age of the system to 0.5–1.0 Myr making the components of θ^1 Ori E some of the youngest intermediate-mass PMS stars known and far younger than stars in the HAeBe phase. θ^1 Ori E is not among the optically brightest stars in the Trapezium, but has long been recognized as the second brightest Trapezium source in X-rays (Ku et al. 1982; Gagne & Caillault 1994; Schulz et al. 2001). The *Chandra* Orion Ultradeep Project (COUP) observed θ^1 Ori E (COUP 732) for a total exposure of about 10 days over a time period of 3 weeks and found a low level of variability including one moderate X-ray flare (Stelzer et al. 2005). Its luminosity during COUP was determined to be $\log L_x[\mathrm{erg\ s^{-1}}] = 32.4$; early *Chandra* High Energy Transmission Grating (HETG) spectra indicated plasma temperatures of up to 50 MK (Schulz et al. 2003).

The HETG Orion Legacy Project has now accumulated almost 4 days of total exposure of θ^1 Ori E allowing for an in depth study of its X-ray spectral properties. The following analysis of θ^1 Ori E's high-resolution X-ray spectrum is aimed to characterize its coronal nature. The existence of coronal X-rays confirms predictions that very young intermediate-mass stars of less than 4 $M_\odot$ are not fully radiative (Palla & Stahler 1993) and may possess some form of magnetic dynamo. We also compare these properties with those observed in θ^2 Ori A, various T Tauri stars including the relatively massive T Tauri star, SU Aur (2 $M_\odot$), active coronal sources, and post-main-sequence-evolved G-type giants. The optical and binary system parameters of θ^1 Ori E can be found in Herbig & Griffin (2006).

2. OBSERVATIONS AND ANALYSIS

2.1. Observations, Data Processing

As part of the HETGS Orion Legacy Project, we have observed θ^1 Ori E on 11 separate occasions from 1999 through 2007, mostly within our HETG Guaranteed Time program, with individual exposure times ranging from about 10–50 ks. The HETGS (Canizares et al. 2005) is an objective transmission grating spectrometer with two channels optimized for high and medium energies (HEG and MEG, respectively). The HEG and MEG spectra of each point source in the field form a shallow "×" centered on the zeroth order image. Since the Orion Trapezium field is crowded, we had to take special care to avoid source confusion when possible and to assess contamination and reject spectra when not. The range in spacecraft roll angles, the redundancy provided by multiple gratings and orders, the narrow point-spread function, and the efficiency of order sorting with the CCD energy resolution all help to provide a reliable spectrum.

We processed the data with CIAO 3.4 (Fruscione et al. 2006) taking care to fine tune the zero order detection to accurately center on θ^1 Ori E. Response files were made with the most recent calibration database available at the time (version 3.4). Further analysis was done using ISIS (Houck & Denicola 2000), an Interactive Spectral Interpretation System for high-resolution X-ray spectroscopy, developed especially for scriptable, extensible analysis of *Chandra* high-resolution spectra.

We give an observing log in Table 1, along with ancillary information and some derived properties of each observation.

2.2. Source Confusion

To assess confusion in detail, we used two techniques. For field source zeroth-order coincidence with the diffracted spectra of θ^1 Ori E, we used the COUP (Getman et al. 2005) source

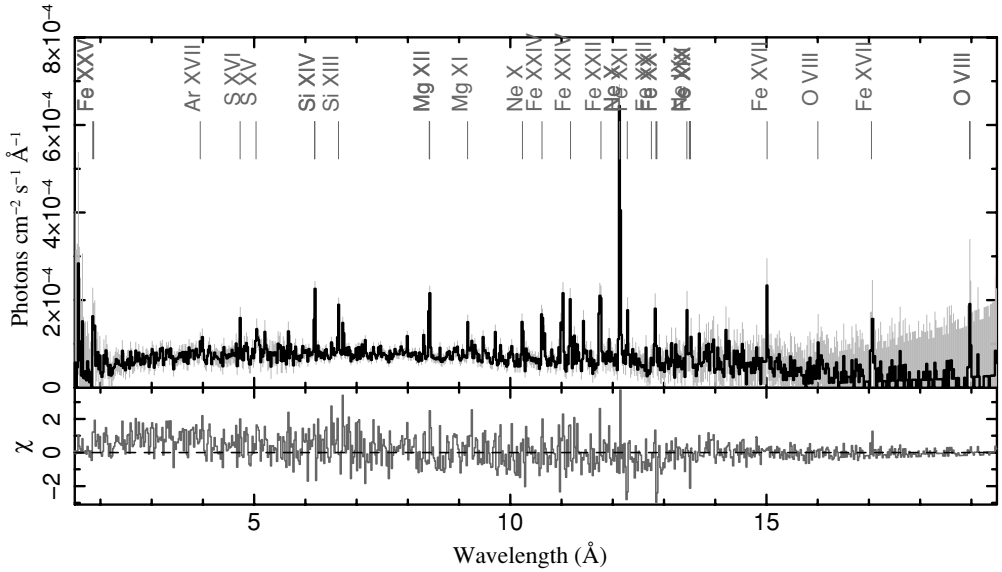

Figure 1. Here is an overview of the cumulative spectrum (about 260 ks) for combined MEG and HEG fluxes, for a bin size of 0.02 Å. Some significant lines are marked. The statistical counting uncertainty is shown in gray. The lower panel shows the residuals against the emission measure model. The integrated flux (1–40 Å) at Earth is 3.3×10^{-12} erg cm^{-2} s^{-1} (1.3×10^{-3} phot cm^{-2} s^{-1}).

list, and for each observation we transformed the list's celestial coordinates to the diffraction coordinate system for θ^1 Ori E. We did not find any source on the spectral regions with significant counts. The second technique assessed the contamination from sources near the zeroth order, such that their diffracted spectra would overlap with the HEG or MEG spectra of θ^1 Ori E, and so close to the zeroth order that the order sorting by CCD energy would distinguish orders. For this, it was crucial to inspect the events' distribution as selected from the θ^1 Ori E default binning region (cross-dispersion region half-width of 6.6×10^{-4} deg) in diffraction distance versus energy (the CCD blurred energy) coordinates in which zeroth orders appear as vertical distributions and diffracted photons as hyperbolas. Here we found significant contamination for a few observations and had to reject all or some orders.

The useful exposure from which we can extract spectra, light curves, and line fluxes totals to 260 ks. Rejected orders or observations are flagged in Table 1. A cumulative counts spectrum is shown in Figure 1.

2.3. Light Curves, Variability

There was little variability of any significance within any observation. The MEG rate was about 0.05 counts s^{-1}. Variations within each observation were consistent with statistical uncertainties—no abrupt increases or slow decays characteristic of coronal flares occurred. Observation to observation, there was also no variability, except for one which had a significantly lower count rate than the others. We show the mean flux rate per observation for MEG and HEG spectra from 2 to 17 Å in the upper left graph in Figure 2, phased using the ephemeris of Herbig & Griffin (2006); values are also listed in Table 1.

2.4. Spectral Analysis

Spectral analysis is an iterative process. For detailed spectral diagnostics and models, accurate line fluxes, centroids, and widths are fundamental to determinations of temperature structure, abundances, and dynamics. However even at HETGS resolution, we are dependent upon plasma models for accurate estimation of the continuum and for assessment of blending. We base our spectral models on the Astrophysical Plasma Emission Database (APED; Smith et al. 2001), ionization balance of Mazzotta et al. (1998), and abundances of Anders & Grevesse (1989). We begin by fitting a one-temperature component model to the short wavelength continuum, then add one or two more components to get a reasonable match to the continuum throughout the spectrum, ignoring strong lines in the process. Next we fit about 100 lines parametrically with unresolved Gaussians folded through the instrumental response, using the line-free plasma model for the local continuum. To improve the statistic per bin, we group the spectra by 2–4 bins and we combined the MEG first orders and combined the HEG first orders, both over all observations, then fit the MEG and HEG jointly. (The default binning oversamples the HEG and MEG resolutions by a factor of 2, or 0.0025 Å and 0.005 Å, respectively.) Combination of spectra is done dynamically—each effective area and redistribution matrix are distinct, and summed counts are compared with the summed folded models to compute the statistic. We adopted an interstellar absorption column of $N_{\rm H} = 2 \times 10^{21}$ cm^{-2} as determined by Schulz et al. (2001). For some weak lines, we froze the wavelength at the theoretical value. This allows us to obtain a limit on the flux which can provide important constraints on emission measure and abundance reconstruction.

After we have mean line fluxes and centroids for a variety of elements and ions (see Table 2), we can reconstruct the emission measure distribution assuming that the plasma has uniform abundances and is in collisional ionization equilibrium. We use a uniform logarithmic temperature grid and minimize the line flux residuals by adjusting the weights in each temperature bin as well as the elemental abundances. Since this is an ill-conditioned problem, we impose a smoothness on the emission measure by using its sum-squared second derivative in a penalty function.

Emission measure reconstruction is also an iterative process. First, we ignore lines with large wavelength residuals relative to their preliminary identification based on expectations of a baseline plasma model, since they are likely misidentified or blended. Then we reconstruct a trial emission measure distribution. Lines with large flux residuals are rejected, since

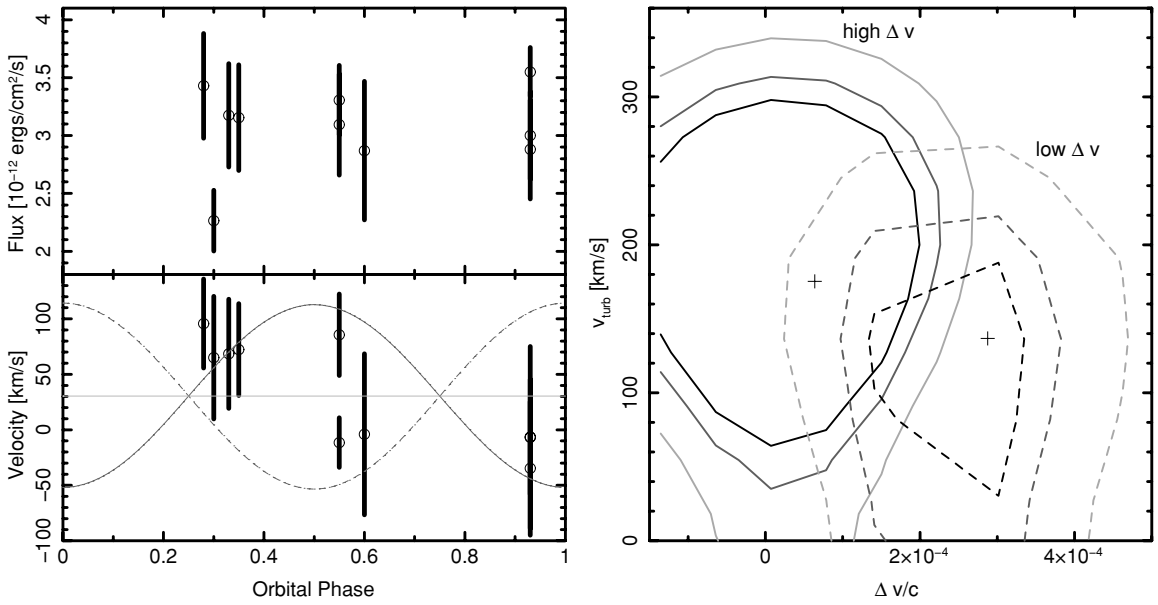

Figure 2. Left panel, top: the circles show the mean fluxes of the HEG and MEG spectra over the wavelength range 2–17 Å for each unconfused observation (see Table 1). Error bars show 3σ uncertainties. Left panel, bottom: circles show the measured radial velocities and 90% uncertainties. Stellar component radial velocities (solid and dashed lines in the lower panel) and orbital phases were computed from the ephemeris and orbital solution of Herbig & Griffin (2006). Right panel: χ^2 confidence contours (1σ, 2σ, and 3σ, inner to outer) for Doppler shift ($\Delta v/c$) against the turbulent broadening parameter. These were computed for two groups of spectra, those nearest the minimum orbital radial velocity separation ("low Δv": dashed), and those nearest the maximum ("high Δv": solid).

they may be symptomatic of unresolved blends or inaccurate emissivities due to uncertainties in the underlying atomic data. We repeat the fit with the accepted lines. We use the emission measure and abundance model to generate a synthetic spectrum and compare to the observed spectrum. Here we can adjust the line-to-continuum ratio by adjusting the normalizations of the emission measure and relative abundances. If the continuum model was improved, we start over by fitting the lines with the improved continuum. Finally, we perform a Monte Carlo series of fits in which we let the measured line flux vary randomly according to its measured uncertainty. This provides an estimate of the uncertainty on the emission measure and the abundances.

We have applied this technique to several other spectra (e.g., see Huenemoerder et al. 2007, and references therein). Given the form of the problem there is no unique solution. However, results can be useful for comparison of emission measures derived with similar methods. Figure 3 shows our reconstructed emission measure distribution whose values are also given in Table 3. The corresponding abundances are shown in Figure 4 and are listed in Table 4.

2.4.1. Dynamics

We searched for dynamical effects by using the mean plasma model spectrum as a template for fitting narrow regions by adjusting the Doppler shift, turbulent broadening velocity, and local normalizations. The 10–12.5 Å region has a number of lines that make it useful for this purpose, and we used that entire wavelength interval in the fits. We fit each observation independently for line-of-sight velocity. The results are listed in Table 1 and shown in Figure 2. The radial velocities are consistent with the orbital velocities of the stellar components—that is, they are generally less than or equal to the orbital radial velocities, but are limited by the spectrometer's sensitivity. According to the orbital solution of Herbig & Griffin (2006), the stellar components have a projected radial velocity amplitude of about 80 km s^{-1} and a systemic velocity of 30 km s^{-1} (note that

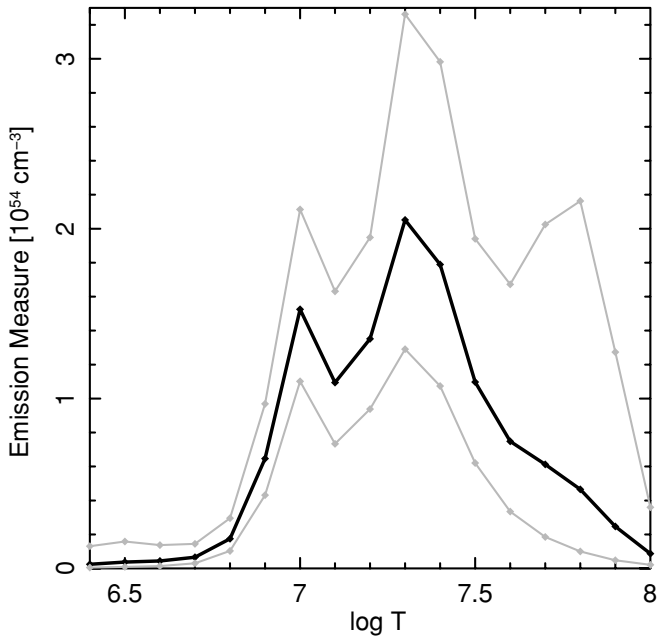

Figure 3. Reconstructed emission measure, for a distance of 450 pc and $N_{\rm H} = 2\times10^{21}$ cm^{-2}. The upper and lower gray boundaries are 1σ (logarithmic) statistical uncertainties from Monte Carlo iterations in which the measured fluxes were perturbed randomly according to their measurement uncertainties. The integrated emission measure is 1.2×10^{55} cm^{-3}.

for the adopted masses of 3.5 $M_\odot$, the inclination is $i = 61°$). While there is a slight systematic offset toward the redshifted component at some phases (e.g., 0.28, 0.30, 0.33, 0.35), the trend does not persist since at other phases (e.g., 0.55, 0.60), measurements span the range between the components' orbital velocities.

To obtain better sensitivity and to examine line widths, we also fit spectra combined into two groups, one nearest to zero velocity separation (near phase 0.25: four observations) and the

Table 2
Line Flux Measurements

Ion	log T_{max} (log K)	λ_{pred} (Å)	λ_{meas}[a] (Å)	f_{meas}[a] (10^{-6} phot cm^{-2} s^{-1})	f_{pred}
Fe XXV	7.8	1.8607	1.8684 (0.0073)	3.293 (1.846)	1.433
Ca XIX	7.5	3.1772	3.1769 (0.0023)	1.135 (0.421)	0.518
Ca XIX	7.4	3.1909	3.1909 (0.0000)	0.033 (0.223)	0.172
Ca XIX	7.5	3.2110	3.2110 (0.0000)	0.373 (0.355)	0.156
Ar XVIII	7.7	3.7338	3.7355 (0.0081)	0.328 (0.351)	0.236
Ar XVII	7.4	3.9491	3.9582 (0.0059)	0.961 (0.558)	0.397
S XV	7.3	4.0883	4.0883 (0.0000)	0.093 (0.226)	0.049
S XVI	7.6	4.7301	4.7272 (0.0026)	1.615 (0.530)	1.030
Si XIV	7.4	4.9468	4.9468 (0.0000)	0.193 (0.311)	0.124
S XV	7.2	5.0387	5.0405 (0.0035)	1.253 (0.556)	1.136
S XV	7.2	5.0648	5.0648 (0.0000)	0.541 (0.499)	0.246
S XV	7.2	5.1015	5.1038 (0.0051)	0.991 (0.505)	0.373
Si XIV	7.4	5.2174	5.2172 (0.0065)	1.371 (0.604)	0.580
Si XIII	7.1	5.4045	5.4045 (0.0000)	0.031 (0.255)	0.131
Si XIII	7.1	5.6805	5.6698 (0.0030)	1.507 (0.511)	0.391
Si XIII	6.9	5.8160	5.8042 (0.0035)	0.815 (0.410)	0.027
Si XIV	7.4	6.1831	6.1825 (0.0008)	4.908 (0.466)	4.143
Si XIII	7.0	6.6480	6.6469 (0.0011)	3.341 (0.426)	2.937
Mg XII	7.2	7.1063	7.1028 (0.0018)	1.095 (0.290)	0.735
Mg XI	6.9	7.3101	7.3101 (0.0000)	0.173 (0.211)	0.044
Fe XXII	7.1	7.6812	7.6812 (0.0000)	0.026 (0.136)	0.073
Al XII	7.0	7.7573	7.7668 (0.0054)	0.521 (0.281)	0.458
Mg XI	6.9	7.8503	7.8503 (0.0000)	0.472 (0.277)	0.257
Al XII	6.9	7.8721	7.8721 (0.0000)	0.608 (0.300)	0.319
Fe XXIII	7.2	7.9009	7.9009 (0.0000)	0.079 (0.181)	0.149
Fe XXIV	7.4	7.9857	7.9794 (0.0138)	0.515 (0.484)	0.523
Fe XXIV	7.4	7.9960	7.9894 (0.0121)	1.055 (0.733)	0.266
Fe XXIII	7.2	8.3038	8.3055 (0.0025)	1.078 (0.346)	0.552
Fe XXIV	7.4	8.3161	8.3217 (0.0022)	0.901 (0.335)	0.581
Fe XXIV	7.4	8.3761	8.3810 (0.0037)	0.321 (0.272)	0.225
Mg XII	7.2	8.4219	8.4215 (0.0008)	5.875 (0.531)	5.198
Fe XXI	7.1	8.5740	8.5643 (0.0056)	0.377 (0.306)	0.295
Fe XXIII	7.2	8.8149	8.8158 (0.0062)	0.357 (0.302)	0.566
Fe XXII	7.1	8.9748	8.9741 (0.0047)	0.811 (0.360)	0.582
Mg XI	6.8	9.1687	9.1710 (0.0015)	2.590 (0.475)	1.866
Fe XXI	7.1	9.1944	9.1944 (0.0000)	0.249 (0.307)	0.220
Fe XXII	7.1	9.3933	9.3865 (0.0150)	0.277 (0.355)	0.126
Ne X	7.0	9.7083	9.7082 (0.0048)	2.002 (0.899)	1.210
Ni XIX	6.8	10.1100	10.1169 (0.0150)	0.018 (0.220)	0.044
Fe XX	7.0	10.1203	10.1332 (0.0032)	0.654 (0.432)	0.194
Ne X	7.0	10.2390	10.2390 (0.0015)	4.084 (0.634)	3.736
Fe XXIV	7.4	10.6190	10.6166 (0.0041)	3.659 (1.812)	3.792
Fe XIX	6.9	10.6491	10.6435 (0.0086)	0.759 (0.764)	0.237
Fe XXIV	7.4	10.6630	10.6650 (0.0027)	2.314 (0.652)	1.990
Fe XXIII	7.2	11.0190	11.0188 (0.0043)	2.517 (1.651)	1.944
Fe XXIV	7.4	11.0290	11.0312 (0.0039)	3.934 (1.563)	2.460
Fe XXIV	7.4	11.1760	11.1764 (0.0015)	6.469 (0.946)	4.445
Fe XVIII	6.8	11.3260	11.3132 (0.0041)	1.337 (0.574)	0.469
Ne IX	6.6	11.5440	11.5436 (0.0060)	0.578 (0.519)	0.560
Fe XXIII	7.2	11.7360	11.7400 (0.0012)	7.656 (1.068)	6.279
Fe XXII	7.1	11.7700	11.7719 (0.0014)	6.244 (0.996)	5.384
Ne X	6.9	12.1348	12.1352 (0.0010)	30.490 (2.300)	25.433
Fe XXIII	7.2	12.1610	12.1610 (0.0000)	4.296 (1.306)	3.492
Fe XVII	6.7	12.2660	12.2713 (0.0053)	2.024 (0.937)	0.900
Fe XX	7.0	13.3850	13.3844 (0.0075)	1.416 (1.071)	0.962
Fe XIX	6.9	13.4230	13.4230 (0.0000)	1.162 (1.131)	0.389
Ne IX	6.6	13.4473	13.4493 (0.0050)	5.083 (2.097)	3.874
Fe XIX	6.9	13.4620	13.4620 (0.0000)	0.893 (1.591)	0.883
Fe XIX	6.9	13.4970	13.4970 (0.0000)	2.554 (1.311)	1.552
Fe XIX	6.9	13.5180	13.5324 (0.0048)	4.074 (1.938)	3.422
Fe XIX	6.9	13.6450	13.6599 (0.0150)	0.609 (0.889)	0.543
Ne IX	6.6	13.6990	13.6927 (0.0043)	3.873 (1.503)	1.714
Fe XIX	6.9	13.7950	13.7986 (0.0109)	1.971 (1.789)	1.361
Fe XVII	6.7	13.8250	13.8351 (0.0052)	3.759 (1.585)	0.718
Fe XVIII	6.8	14.2080	14.2132 (0.0037)	6.378 (1.987)	5.219

Table 2
(Continued)

Ion	log T_{max} (log K)	λ_{pred} (Å)	λ_{meas}[a] (Å)	f_{meas}[a] (10^{-6} phot cm^{-2} s^{-1})	f_{pred}
Fe XVIII	6.8	14.2560	14.2560 (0.0000)	0.442 (1.192)	0.996
Fe XX	7.0	14.2670	14.2670 (0.0000)	3.975 (2.142)	1.300
Fe XVIII	6.8	14.3430	14.3430 (0.0000)	0.323 (0.727)	0.618
Fe XVIII	6.8	14.3730	14.3730 (0.0000)	1.205 (1.127)	1.325
Fe XVIII	6.8	14.5340	14.5355 (0.0050)	3.860 (1.546)	1.003
Fe XVII	6.7	15.0140	15.0109 (0.0022)	10.500 (2.349)	8.749
Fe XIX	6.9	15.0790	15.0825 (0.0068)	2.224 (1.393)	1.098
O VIII	6.7	15.1762	15.1680 (0.0075)	1.598 (1.276)	0.664
Fe XIX	6.9	15.1980	15.2082 (0.0058)	2.238 (1.398)	0.928
Fe XVII	6.7	15.2610	15.2600 (0.0061)	2.795 (1.488)	2.462
Fe XVIII	6.8	15.8700	15.8572 (0.0039)	2.800 (1.661)	0.432
Fe XVIII	6.8	16.0710	16.0814 (0.0058)	2.960 (1.796)	1.813
Fe XVII	6.7	16.7800	16.7650 (0.0029)	3.114 (2.137)	3.792
Fe XVII	6.7	17.0510	17.0547 (0.0041)	10.810 (3.391)	4.557
Fe XVII	6.7	17.0960	17.1011 (0.0048)	6.809 (2.930)	4.086
Fe XVIII	6.8	17.6230	17.6080 (0.0025)	4.326 (2.586)	1.323
O VII	6.4	17.7680	17.7680 (0.0000)	0.300 (0.315)	0.041
O VII	6.4	18.6270	18.6270 (0.0000)	0.900 (0.926)	0.123
O VIII	6.7	18.9698	18.9744 (0.0043)	17.680 (5.846)	13.292

Notes. These are the lines that were used in the emission measure and abundance reconstruction. The f_{pred}, is what the emission measure and abundance model predicts.
[a] Values in parentheses are 1σ uncertainties. If the uncertainty for the wavelength is 0.0, then the line position was frozen in the fit.

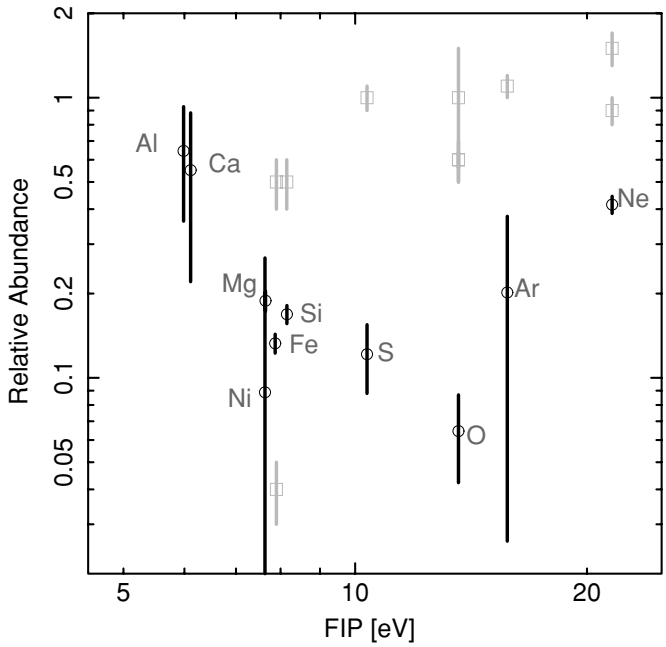

Figure 4. θ^1 Ori E abundances (circles) relative to solar photospheric values (Anders & Grevesse 1989) as derived from emission measure reconstruction. Error bars give the statistical 1σ uncertainty. Light colored squares give Orion stellar photospheric (Cunha et al. 1998, 2006; Cunha & Lambert 1994; Cunha & Smith 2005) or nebular (Esteban et al. 2004) abundance ratios for Fe, Si, S, O, Ar, and Ne.

other nearest to maximum velocity separation (near phase 0.5 or 1.0: six observations). We computed contour maps in line-of-sight and turbulent broadening velocities. The point of this is not necessarily that we expect turbulent broadening, but that there could be broadening due to binary orbital effects, and fitting turbulent broadening is simply a useful parameterization of this. For instance, for equally X-ray bright stars, the X-ray line's

Table 3
Emission Measure Model

log T (log K)	EM	EM_{low} (10^{54}cm^{-3})	EM_{high}
6.4	2.45e-02	4.60e-03	1.31e-01
6.5	3.76e-02	8.90e-03	1.59e-01
6.6	4.40e-02	1.41e-02	1.37e-01
6.7	6.59e-02	3.00e-02	1.45e-01
6.8	1.74e-01	1.03e-01	2.96e-01
6.9	6.46e-01	4.31e-01	9.69e-01
7.0	1.53e+00	1.10e+00	2.11e+00
7.1	1.09e+00	7.33e-01	1.63e+00
7.2	1.35e+00	9.38e-01	1.95e+00
7.3	2.05e+00	1.29e+00	3.26e+00
7.4	1.79e+00	1.07e+00	2.98e+00
7.5	1.10e+00	6.21e-01	1.94e+00
7.6	7.48e-01	3.35e-01	1.67e+00
7.7	6.13e-01	1.85e-01	2.02e+00
7.8	4.65e-01	1.00e-01	2.16e+00
7.9	2.47e-01	4.79e-02	1.27e+00
8.0	8.67e-02	2.09e-02	3.60e-01

Notes. The reconstructed emission measure over the temperature range of sensitive features. The "low" and "high" values are the logarithmic 1σ boundaries from Monte Carlo iterations.

measured radial velocity could always be zero (or the systemic value), but the lines could broaden and narrow, modulated by the orbital radial velocity. If only one star were the X-ray source, the lines could shift but maintain a constant width. Since we are photon limited, we need to group spectra in order to obtain significant counting statistics.

The resulting confidence contours are shown in Figure 2. We see the radial velocity offset toward a small positive velocity as we should in the low-Δv group at a level of about 30–120 km s^{-1} (or $\Delta v/c \sim 1$–4×10^{-4}; 90% confidence limits), while the high-Δv group range is -60 to 60 km s^{-1}. Broadening is marginally significant with 90% confidence contours of 60–300 km s^{-1} for the high-Δv group and 0–200 km s^{-1} for the low-Δv group (with a 1σ lower limit of 20 km s^{-1}).

2.4.2. He-like Triplets

The HETGS bandpass includes the He-like triplet lines of Mg XI, Ne IX, and O VII, which are useful diagnostics of density in the coronal regime (Gabriel & Jordan 1969, 1973). Due to the absorption toward Orion and the low sensitivity of the HETGS at 22 Å, we have no useful data on O VII, but we do have spectra of Mg XI and Ne IX. By fitting the line ratios of the resonance (r), intercombination (i), and forbidden (f) lines we are able to put upper limits on the coronal electron density. In our fits, we constrained the relative positions of the triplet components and included blends as estimated from the emission measure model spectrum. The Ne X Lyman series converges near the Mg XI i-line (9.230 Å). We included relevant lines of this series by providing an initial guess for their strengths by scaling fluxes according to their relative f-values from the isolated and well-detected Ly-γ and δ lines, since APED does not contain lines with upper levels $n > 5$. The locations of the weaker and blended features are 9.215 Å (Ne X Ly-α series $n = 9$ to $n = 1$ transition), 9.246 Å (Ne X 8-to-1 transition), and 9.194 Å (Fe XXI). The weakest (Fe XXI) line's position was frozen, while positions and fluxes of the others were left free and gave reasonable fitted wavelengths. While this is not a complete and accurate plasma model for the region, it is a useful parameterization to obtain ratios for the interesting features.

Table 4
Relative Elemental Abundances

Element	Abundance[a]	FIP[b] (eV)
O	0.06 (0.03)	13.618
Ne	0.42 (0.03)	21.564
Mg	0.19 (0.02)	7.646
Al	0.64 (0.28)	5.986
Si	0.17 (0.01)	8.151
S	0.12 (0.03)	10.360
Ar	0.20 (0.17)	15.759
Ca	0.55 (0.33)	6.113
Fe	0.13 (0.01)	7.870
Ni	0.14 (0.14)	7.635

Notes. Uncertainties in "()" are 1σ values.
[a] Abundances are relative to solar using the values of Anders & Grevesse (1989).
[b] FIP is the first ionization potential.

There are Fe blends in the Ne IX triplet region, but since the Ne:Fe abundance ratio is high (see Table 4), these are not severe.

The continuum in each region was evaluated from the plasma model and not governed by free parameters.

Results for both triplets are consistent with low density. In Figure 5, we show the spectra and confidence contours of the G and R ratios, defined as $G = (f + i)/r$ and $R = f/i$. G is primarily a function of temperature, and R of density. The density and temperature dependences are from APEC calculations (Smith et al. 2001).[3]

2.4.3. Abundance Ratios

By forming appropriately weighted flux ratios of line pairs, we can obtain relatively temperature-insensitive abundance ratios. This is achieved by relating a linear combination of emissivities of He- and H-like resonance lines for one element to a similar linear combination of another element, so as to minimize fluctuations with temperature in their ratio. If this ratio is constant, then the analogous combination of line fluxes gives the abundance ratio. This technique was explained in detail by Liefke et al. (2008) and described generally by García-Alvarez et al. (2005).

We define the ratio in the following way:

$$r = \frac{F_{1,1} + a_1 F_{1,2}}{F_{2,1} + a_2 F_{2,2}} = \frac{A_1 a_0}{A_2} \frac{\int [\epsilon_{1,1}(T) + a_1 \epsilon_{1,2}(T)] D(T)\, dT}{\int [\epsilon_{2,1}(T) + a_2 \epsilon_{2,2}(T)] D(T)\, dT} \quad (1)$$

in which subscripts i, j on F refer to the line j from element i, F is the observed flux, $\epsilon(T)$ is the emissivity, $D(T)$ is the emission measure, and A_i is the abundance of element i. The parameters, a_n, are to be determined. It is clear that if the terms in square brackets within the integrals are identical in numerator and denominator for all T, then the integrals cancel and we are left with the abundance ratio (parameters a_1 and a_2 serve to flatten the ratio, and a_0 normalizes it). We determined the parameters by minimizing the variation in the ratios using H-like and He-like line emissivities from the APED database. Rewriting in terms of the abundance ratio for these lines, we have

$$\frac{A_1}{A_2} = \left(\frac{1}{a_0}\right) \frac{F_{1,\mathrm{H}} + a_1 F_{1,\mathrm{He}}}{F_{2,\mathrm{H}} + a_2 F_{2,\mathrm{He}}} \quad (2)$$

[3] Data for the lines are available from http://cxc.harvard.edu/atomdb/features/denHETG.ps.

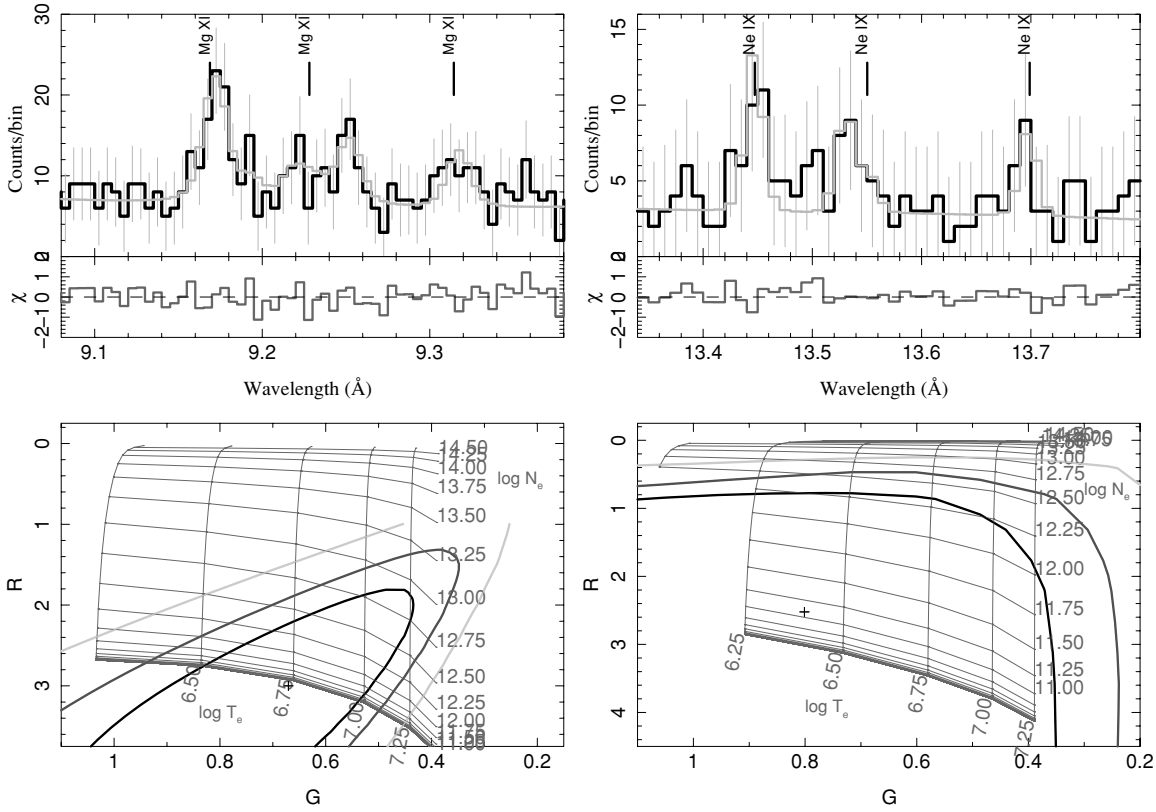

Figure 5. Upper plots show the Mg XI (left) and Ne IX (right) triplets counts spectra (black histogram), a multi-Gaussian fit (gray line), and residuals (lower panels of top plots). The positions of the triplet components are marked. The lower plots show the fits to the G ($= (f + i)/r$) and R ($= f/i$) ratios, which are primarily temperature and density sensitive, respectively, as given by the grid. The contours are the 1σ, 2σ, and 3σ levels from lower/inner to upper/outer contours.

Table 5
Temperature Insensitive Ratio Coefficients

Ratio	a_0	a_1	a_2	σ
Ne:Mg	1.440	0.050	2.675	0.273
Mg:Si	0.536	0.085	1.920	0.064
Si:S	1.197	0.125	1.545	0.092
S:O	0.212	2.990	0.000	0.137
Ne:O	0.347	2.590	0.000	0.120

Notes. The coefficients are to be used as defined by Equation (2). The last column, σ, is the standard deviation of the emissivity ratio, which is never perfectly flat, and coefficient a_0 represents the mean of the ratio.

Table 6
Abundance Ratios[a]

Elements	$r(T_{\rm insens})$	r(EM)
Ne:Mg	1.7 (0.3)	2.2 (0.2)
Mg:Si	1.0 (0.1)	1.1 (0.1)
Si:S	1.2 (0.2)	1.4 (0.4)
S:O	1.4 (1.0)	1.9 (0.8)
Ne:O	4.9 (2.8)	6.5 (2.3)
Mg:O[b]	2.9 (1.8)	2.9 (1.0)
Si:O[b]	1.8 (0.9)	2.6 (0.9)

Notes. $r(T_{\rm insens})$ gives the abundance ratios from the temperature–insensitive method, while r(EM) gives ratios from the emission measure reconstruction (see Table 4). Values in parentheses are 1σ statistical uncertainties.

[a] The ratios are of relative solar photospheric abundances.

[b] Derived from preceding ratios—not determined directly.

in which subscripts H and He represent the hydrogen-like Lyman-α doublet and the helium-like Lyman-α resonance line, respectively. We tabulate coefficients for a few useful ratios in Table 5 as derived from APED for units of F in (phot cm^{-2} s^{-1}) and abundances relative to solar. Minimization of the ratio variances were restricted to temperature ranges where the emissivities were greater than 1% of their maximum. In Table 6, we give the abundance ratios derived from the temperature–insensitive ratios along with values from emission measure modeling. The ratios from each method are in very good agreement. This means that abundance ratios can be derived fairly easily, without resorting to emission measure reconstruction.

3. DISCUSSION, INTERPRETATION

The recent determination by Herbig & Griffin (2006) that θ^1 Ori E is a moderate mass PMS spectroscopic binary is very important in the context of stellar evolution and X-ray activity. When θ^1 Ori E arrives on the main sequence, we expect it to be faint or non-detectable in soft X-rays. Yet at the age of 0.5 Myr, it is the second-brightest steady X-ray source in the Orion Trapezium. The binary system has $L_x = 1.2 \times 10^{32}$ erg s^{-1}, and given an optical luminosity of 29 $L_\odot$ (Herbig & Griffin 2006) it thus has $L_x/L_{\rm bol} = 10^{-3}$ for the pair. This value is near the saturation limit of coronally active stars (Prosser et al. 1996). The X-ray emission is similar to other magnetically active stars, having a broad temperature distribution and narrow emission lines. Hence we surmise that θ^1 Ori E has dynamo activity and probably has strong convection zones. This is also

in accordance with evolutionary models of stellar interiors (Siess et al. 2000) which indicate a substantial convection zone for stars like the θ^1 Ori E components (also see Figure 1 of Stelzer et al. 2005).

Prior to the Herbig & Griffin (2006) determination that θ^1 Ori E is a binary of G-type stars, θ^1 Ori E was considered to be a B5 star. Schulz et al. (2003) considered the X-rays to be a hybrid of wind shock emission and magnetically confined winds, but they did note a striking similarity to active coronal sources. Stelzer et al. (2005) interpreted the emission as from a weak wind, but noted unusual emission characteristics, such as due to an extended magnetosphere and magnetically confined wind shocks. It is now clear in hindsight, given the spectral types, that emission is coronal in nature.

θ^1 Ori E did not show any distinct flares during our observations, which is somewhat unusual for coronally active stars. This lack of activity is consistent, however, with the long intervals of the constant flux seen by Stelzer et al. (2005). There was one observation in which the flux was *lower* than our average (see Figure 2) and examination of the spectra shows that this is manifested in diminished short wavelength flux (below about 10 Å). This variation between observations cannot be attributed to rotational phase dependence since it does not repeat. We also found no significant variability within any of our observations. It is possible that the system is so coronally active that a significant proportion of the average flux is from continuously visible flares, which would also give rise to the dominant emission measure peak at $\log T = 7.3$, but one observation had a bit less flaring.

The HETGS flux was about half that reported by Stelzer et al. (2005) from heavily piled, low-resolution spectra. The HETGS flux calibration is accurate to about 5%. Since flux for our observations was effectively constant and spans the time of the COUP observations, the difference in flux without obvious flares is unusual. Since the Stelzer et al. (2005) analysis was made difficult by the high photon pileup in the core of θ^1 Ori E, they resorted to spectral analysis of photons only from the wings of the point-spread function. We reanalyzed spectra for θ^1 Ori E from one of the COUP data sets, observation ID 4373, for which the flux was constant. We used an extraction radius of 2.25 arcsec centered on the source, including piled photons and made standard responses for the region. To fit the spectrum, we used the pileup model of Davis (2001) as implemented in ISIS. Pileup is a very nonlinear process; there can be multiple solutions since the count rate first saturates with increasing fluence, then can decrease as events are rejected from telemetry. Finally, for extremely high pileup, the count rate can again increase when the core is fully saturated and the wings grow. We used two-temperature component, absorbed APED plasma models, similar to those of Stelzer et al. (2005), and used Monte Carlo techniques to explore parameter space, given the multi-valued nature of pileup fitting and the possibly degenerate nature of the models. While we found solutions with fluxes similar to those presented by Stelzer et al. (2005), we found equally acceptable solutions (reduced $\chi^2 < 1.3$) with fluxes comparable to our HETGS-derived values. Incidentally, all our fits to this one spectrum preferred $N_{\rm H} \gtrsim 3 \times 10^{21}$ cm^{-2}, a bit larger than our adopted value of 2×10^{21} cm^{-2}. We conclude that the Stelzer et al. (2005) flux is probably in error and the source is probably steady outside of distinct flares with a flux of about 3×10^{-12} erg cm^{-2} s^{-1}.

The radial velocities determined from lines are consistent with the orbital dynamics. Given a peak-to-peak orbital radial velocity amplitude of 160 km s^{-1}, we have marginal sensitivity for detection of the orbital modulation if emission were dominated by one stellar component (see the confidence limits in Table 1 and Figure 2). Variability over the time period of observations could destroy any orbital systematic radial velocities in X-ray lines if the relative activity level of the two stellar components changed. Our phase coverage is also poor, but the lack of significant velocity offsets at phases of maximum orbital velocity separation suggests that both stellar components are roughly equal in X-ray emission. The marginal detection of line broadening, particularly at these same phases, is consistent with the broadening being due to orbital velocity effects. We conclude that the lines are similar to other coronal sources—narrow, and effectively unresolved.

The absolute abundances are rather low when compared to other coronal sources. If we compare θ^1 Ori E to the abundances derived from low-resolution COUP spectra of Maggio et al. (2007), they are not only lower by a factor of 5 or more in general, the ratios are also different—they are, in fact, uncorrelated. This probably has as much to do with different methods and spectral resolutions than with intrinsic differences between θ^1 Ori E and average Orion stars. Maggio et al. (2007) use two temperature component fits, and these cannot accurately reproduce abundances and emission measures for realistic, continuous emission measure distribution plasmas. If a fitted temperature component is off the peak of some ion's temperature of peak emissivity, and there is actually plasma at that temperature, then a two-temperature model will artificially increase the abundance of that element in order to reproduce the flux. Comparison of low- and high-resolution results with different modeling approach is in general not meaningful.

3.1. Loop Sizes

The geometric structure of stellar coronae is largely an open question, and is relevant to energetics, variability, and likelihood of interactions with stellar companions or disks. While there are many uncertain parameters, we can provide order-of-magnitude estimates via several methods to show that loops could be compact (small fraction of the stellar radii of $7R_\odot$; see Table 7), or comparable to the stellar radii and thus a significant fraction of the stellar separation (the semimajor axis is about $2.5R_*$; see Herbig & Griffin 2006).

If we assume that the X-ray emission originates in an ensemble of identical semi-circular loops, we can estimate the order of magnitude of the loops' radius. The loop radius (or height if vertically oriented) relative to the stellar radius can be expressed as

$$h = E_{51}^{1/3} R_{10}^{-1} n_{10}^{-2/3} N_2^{-1/3} \alpha_{-1}^{-2/3} \quad (3)$$

in which E is the volume emission measure, R is the stellar radius, N is the number of identical loops, n is the electron density, and α is the loop aspect ratio (cross-sectional radius to height, $\leqslant 1$), and the subscripts indicate the power of 10 scale factor (all cgs or unit-less quantities). Only two of these parameters are well determined: $E = 1.2 \times 10^{55}$ cm^{-3} from our X-ray spectral modeling and $R \sim 5 \times 10^{11}$ cm from the radial velocity curve analysis of Herbig & Griffin (2006). Densities are poorly constrained; we will adopt 10^{12} cm^{-3} for argument (see Figure 5). From solar loops, α is about 0.1, and given the lack of variability in θ^1 Ori E (to about 10% accuracy; see Figure 2), we will let $N = 100$. If we assume that the emission is divided

Table 7
Stellar Comparison

Quantity	θ^1 Ori E [a]	SU Aur	AB Aur	μ Vel	HR 9024[b]	Capella Aa[c]
Spec. Type.	G8 III+G8 III	G2 IV	A0	G5 III	G1 III	G8 III
$T_{\rm eff}$ (K)	5012	5550	9750	5030	5530	5000
Age (My)	0.5	4	4	360	Post-ms	525
$M/M_\odot$	3.5	2.0	2.7	3	2.9	2.7
$R/R_\odot$	7	2.6	2.3	14.4	13.6	12.2
$g/g_\odot$	0.07	0.3	0.5	0.01	0.02	0.02
P (day)	9.9	1.8	1.4:	117	23.2	104
$v \sin i$ (km s^{-1})	37	66	80	6.2	22	5
$L_{\rm bol}/L_\odot$	29	6.3	49	108	90	78.5
$L_x/10^{30}$ (erg s^{-1})	121	8	0.4	2.2	63,125	1.6
$(L_x/L_{\rm bol})/10^{-6}$	1100	300	2	5.4	181,360	5.3
$VEM/10^{52}$ (cm^{-3})	1200	50	5	8	200,800	4
$\overline{T}_x$ (MK)[d]	20	20	4.7	7.9	30,80	6.3
A(Fe)[e]	0.1	0.6	0.3	1.8	0.2,0.7	0.8
A(O)[e]	0.1	0.3	0.2	0.7	0.6,1.1	0.4
A(Ne)[e]	0.4	1.3	0.6	1.4	1.1,1.2	0.7

Notes. θ^1 **Ori E:** Herbig & Griffin (2006); this paper. **SU Aur:** Franciosini et al. (2007); Robrade & Schmitt (2006); DeWarf et al. (2003). **AB Aur:** Telleschi et al. (2007). μ **Vel:** Ayres et al. (2007); Wood et al. (2005). **HR 9024:** Ayres et al. (2007); Testa et al. (2007). **Capella:** Ishibashi et al. (2006); Canizares et al. (2000); Hummel et al. (1994); Ness et al. (2003); Gu et al. (2006).

[a] X-ray properties are for the binary system; if each stellar component contributes equally, values should be divided by two.

[b] When two quantities are given they are for quiescent and flare states, respectively.

[c] X-ray properties assume that component Aa dominates.

[d] A qualitative temperature of the high energy emission measure distribution, adopted from visual inspection of published curves or few-T fits.

[e] Abundances are relative to solar.

equally between the two binary stellar components, then with these parameters we obtain $h \sim 0.02$, implying that the coronae are compact. For a density of 10^{10} cm^{-3}, this height increases by a factor of 20 to about 0.4, a significant fraction of the orbital separation.

We can also estimate loop parameters using hydrodynamical models from the flare temporal and spectral properties. Assuming that a single flaring loop dominates the emission, Reale (2007) expressed the loop size (his Equation (12)) as $L_9 \sim 3(T_0/T_M)^2\, T_{0,7}^{1/2}\, \tau_{M,3}$. Here L_9 is the loop half-length in units of 10^9 cm, T_0 is the maximum temperature during the flare (and $T_{0,7}$ is the same in units of 10^7 K), T_M is the temperature at which maximum density occurs, and $\tau_{M,3}$ is the time from flare start (in ks) at which maximum density occurs. To apply such a model in detail, we would need the evolution of emission measure (a proxy for density) and temperature (from time-resolved spectra) from the rise to the decay of a flare. We do not have such, so we will make some reasonable approximations to obtain an order-of-magnitude hydrodynamical loop size.

The COUP observation of θ^1 Ori E detected a flare (Stelzer et al. 2005); from this, we estimate that $\tau_{m,3} = 25$. We have an emission measure distribution; we assume that the hotter peak and hot tail represent the integrated history over many flares. From time-resolved analyses of other stars, we have seen that such a hot peak can be directly attributed to flaring (Huenemoerder et al. 2001; Güdel et al. 2004). We will thus assume that the flare mean temperature of maximum density (or maximum emission measure) corresponds to our strongest peak, or $\log T_M = 7.3$ (see Figure 3). We will assume that the hot tail of the EMD represents the maximum flare temperature. This is less well defined, and we adopt $\log T_0 = 7.8$, which is where there is an inflection in our EMD. From these parameters we find a relative loop half-length of about 3.8 stellar radii, or a height (for semi-circular vertical loops) of 2.4 stellar radii.

We can also adopt flare parameters from other giant stars, such as HR 9024 (Testa et al. 2007; see also Table 7), for which $\log T_0 = 7.9$ and $T_0/T_M = 1.4$. Thus, if θ^1 Ori E flare temperatures and densities are similar to those on HR 9024, the loop half-length is about 1 stellar radius (or a height of 0.6 stellar radii).

Since these are order-of-magnitude estimates, we conclude that flare loops can be of order the stellar radius. In sum, an origin of the emission from magnetically confined coronal loops is not unreasonable. To better determine the coronal geometry, more information is needed, such as more stringent constraints on density, detection of rotational modulation, or time-resolved spectroscopy of a large flare.

4. COMPARISON TO OTHER STARS

To understand the nature of the X-ray emission from θ^1 Ori E, we must examine it in the evolutionary context of stars of similar mass. We have collected information for several other stars, both pre-main-sequence and post-main-sequence, with masses ranging from 2 $M_\odot$ to 3.5 $M_\odot$. Information and sources are listed in Table 7 and in Figure 6 we show the objects on a temperature–luminosity diagram along with evolutionary tracks. Of the sample, θ^1 Ori E has the highest relative X-ray luminosity, being as high in $L_x/L_{\rm bol}$ as "saturated" short period active binaries (Vilhu & Rucinski 1983; Cruddace & Dupree 1984; Prosser et al. 1996), even though its period is somewhat longer than those systems. If we look to the future of θ^1 Ori E's evolution and consider AB Aur, we see that $L_x/L_{\rm bol}$ may become much

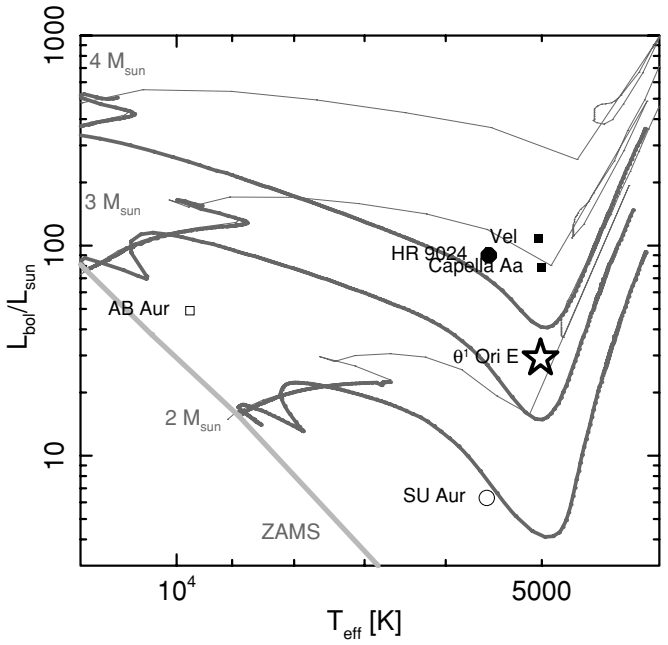

Figure 6. Stars listed in Table 7 are shown on a temperature–luminosity diagram. Pre-main-sequence stars are shown with open symbols and post-main-sequence stars are shown as solid symbols. The shapes encode $L_x/L_{\rm bol}$ as a "star" for $\geqslant 10^{-3}$, circle for $\geqslant 10^{-4}$ to $< 10^{-3}$, and a square for $< 10^{-5}$ (see Table 7 for values). The PMS evolutionary tracks (thick gray lines) and ZAMS are from Siess et al. (2000). The post-main-sequence tracks (thin gray lines) are from Schaller et al. (1992). The tracks are shown for 2 $M_\odot$, 3 $M_\odot$, and 4 $M_\odot$. The post-main-sequence tracks were scaled slightly (0%–3% in temperature, 8%–12% in luminosity) to better coincide with the PMS tracks.)

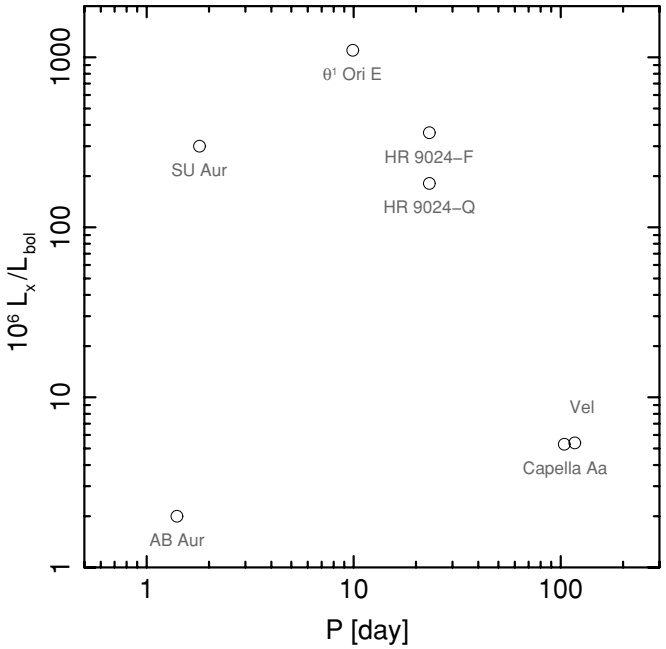

Figure 7. Normalized X-ray luminosity for stars listed in Table 7 are shown as a function of their periods. The stars largely follow an expected rotation-activity trend, except for AB Aur, which is an A-star near the main sequence and is expected to be faint in X-rays. $L_x/L_{\rm bol}$ for θ^1 Ori E is for the system; if each stellar component contributes equally, its value should be divided by two.

smaller; we expect main-sequence A-type stars to be very faint or undetected in X-rays (for reference, a spectral type A0 V star has a mass of $\sim$2 $M_\odot$, and a B5 V of $\sim$6 $M_\odot$).

Stellar rotation is well known to be a key factor in magnetic dynamo generation. If we compare the sample's X-ray activity as a function of period (Figure 7), excluding AB Aur, we see a strong anti-correlation which holds for both pre- and post-main-sequence objects. This is similar to the behavior of active giants, binaries, or main-sequence late-type stellar coronae (Walter & Bowyer 1981; Pizzolato et al. 2003; Gondoin 2005). AB Aur, in spite of its short period, has very low activity; it is approaching the low-activity main-sequence era of its life, and may have a radically different emission mechanism, such as from wind or accretion effects, with lower L_x and X-ray temperatures (Telleschi et al. 2007). Its convective zone, necessary for magnetic dynamo generation, is quite small, being less than 1% of the stellar radius, compared to about 20% for the other stars (Siess et al. 2000, 2005, their Figure 1), so it is reasonable to exclude it from period-activity relations of stars with significant convective regions. θ^1 Ori E has a very hot corona, characterized by an emission measure distribution with a strong peak at about 20 MK (see Figure 3). It is similar to SU Aur and HR 9024 (see Table 7), two objects that displayed strong flares during their X-ray observations. A hot emission measure peak has been directly identified with flares (Huenemoerder et al. 2001; Güdel et al. 2004). In this context, it is curious that during all the COUP and HETG exposures, only one distinct flare was seen (Stelzer et al. 2005). We can only speculate that perhaps θ^1 Ori E is so active that the flare rate is so high that they are nearly always superimposed and create a nearly constant flux. Such was found plausible for Orion's low-mass stars by Caramazza et al. (2007). Our single low-flux HETGS observation (see Figure 2) did have a relative deficit in a short wavelength flux (< 5 Å), a region sensitive to the highest temperature plasmas; it is consistent with diminished flare activity. To sustain continuous flaring, there has to be a continuous source of erupting magnetic fields and their reconnection. The pressure scale height for a hot, low-density plasma is a significant fraction of the binary stellar separation of θ^1 Ori E. There could be star-to-star magnetic reconnections sustained at a fairly high level by the binary proximity and dynamo action generating sufficiently large loops.

The presence of a very hot corona and the low probability of distinct flares is common to several evolved giants, such as HR 9024, μ Vel, 31 Com, or IM Peg (Testa et al. 2007, 2004; Ayres et al. 2007). While this is not understood, it could be a significant trait of the coronal heating mechanisms.

Another distinguishing characteristic of θ^1 Ori E is the relatively low mean metal abundance. Table 4 shows relative elemental abundances from the EMD analysis. All abundances are significantly below unity with oxygen at an extremely low value. When compared to abundances deduced in a similar analysis of θ^1 Ori C (Schulz et al. 2003), its massive neighbor within the Orion Trapezium, then there are a few remarkable differences to note. Values for Ne, Al, and Ca seem very similar within uncertainties, while Mg, Si, S, and Ar are very different, being near or above unity in θ^1 Ori C; values for O and Fe are even lower than in θ^1 Ori C. Figure 4 also compares coronal with average Orion stellar photospheric and nebular values. Since the photospheric and nebular abundances are all near unity, it seems that abundances from the hot X-ray plasmas are fundamentally different. A two-temperature modeling of θ^1 Ori C could reconcile deficient O and Ne values by requiring a significantly higher column density (Gagné et al. 2005), as would forcing the Ne/O ratio to be similar to other coronae (Drake & Testa 2005), though Fe would still remain low. In the case of θ^1 Ori E, the application of a higher column will not change the

low values for Mg and higher-Z elements, but also not enough for O, which at $A(O) = 0.06$ is extremely low. We also find that multi-temperature plasmas more accurately describe the spectra in both stars and thus see trends in Orion Trapezium stars which include some neon deficiency but clearly hot plasmas with low iron and oxygen abundances. For PMS stars, depletion of metals has been explained by formation of dust in the disk, and the remaining gas, seen heated to X-ray temperatures in an accretion shock, is the metal-poor material (Drake et al. 2005). Magnetic coronae generally show low metals, but tend to have higher Ne and O (e.g., II Peg, Huenemoerder et al. 2001; or HR 1099, Drake et al. 2001). Hot plasmas of Orion's stars, if the two studied are representative, seem to be different. There is no theoretical explanation for coronal abundances, but these differences may be clues to fractionation mechanisms.

5. CONCLUSIONS

θ^1 Ori E is perhaps the only case known of a PMS 3 solar mass G-star binary. As such, it holds an important place in our understanding of X-ray dynamo generation and evolution. We believe that when it reaches the main sequence, it will emit a negligible fraction of its luminosity in X-rays. Yet now it is the second brightest X-ray source in the Trapezium. Furthermore, its relative X-ray luminosity ($L_x/L_{\rm bol}$) makes it as strong as any of the coronally active binaries. Thus we conclude that as moderate mass stars collapse toward the main sequence, they go through a phase of strong magnetic dynamo generation, very similar or identical to that of coronally active late-type stars which sustain a convective zone and shear-generated magnetic dynamo. Since A-stars are dark or at most quite faint in X-rays (Schröder & Schmitt 2007), at some point, the dynamo vanishes, and the magnetic fields dissipate. AB Aur, which is near the main sequence and relatively faint in X-rays, is a possible future state of θ^1 Ori E. It is also clear from the post-main-sequence objects that a dynamo can be generated as stars of this mass evolve into giants.

Hot plasma abundances of θ^1 Ori E (as well as of θ^1 Ori C) are different from coronally active stars. θ^1 Ori E is hot and has fairly steady X-ray emission. The high temperature is either due to unresolved flares, or to an unknown mechanism which also may be common to other active G-giants. The temperature structure, abundances, and low variability may be clues to plasma heating mechanisms. Continuing high-resolution spectroscopic studies of Orion stars will show us if some of these patterns are common in the Orion Nebular Cluster.

Support for this work was provided by the National Aeronautics and Space Administration through the Smithsonian Astrophysical Observatory contract SV3-73016 to MIT for Support of the *Chandra* X-Ray Center, which is operated by the Smithsonian Astrophysical Observatory for and on behalf of the National Aeronautics Space Administration under contract NAS8-03060.

Facilities: CXO (HETGS)

REFERENCES

Acke, B., & Waelkens, C. 2004, A&A, 427, 1009
Anders, E., & Grevesse, N. 1989, Geochim. Cosmochim. Acta, 53, 197
Ayres, T. R., Hodges-Kluck, E., & Brown, A. 2007, ApJS, 171, 304
Baines, D., Oudmaijer, R. D., Porter, J. M., & Pozzo, M. 2006, MNRAS, 367, 737
Blondel, P. F. C., & Djie, H. R. E. T. A. 2006, A&A, 456, 1045
Canizares, C. R., et al. 2000, ApJ, 539, L41
Canizares, C. R., et al. 2005, PASP, 117, 1144
Caramazza, M., Flaccomio, E., Micela, G., Reale, F., Wolk, S. J., & Feigelson, E. D. 2007, A&A, 471, 645
Cruddace, R. G., & Dupree, A. K. 1984, ApJ, 277, 263
Cunha, K., Hubeny, I., & Lanz, T. 2006, ApJ, 647, L143
Cunha, K., & Lambert, D. L. 1994, ApJ, 426, 170
Cunha, K., & Smith, V. V. 2005, ApJ, 626, 425
Cunha, K., Smith, V. V., & Lambert, D. L. 1998, ApJ, 493, 195
Damiani, F., Micela, G., Sciortino, S., & Harnden, F. R., Jr. 1994, ApJ, 436, 807
Davis, J. E. 2001, ApJ, 562, 575
DeWarf, L. E., Sepinsky, J. F., Guinan, E. F., Ribas, I., & Nadalin, I. 2003, ApJ, 590, 357
Drake, J. J., Brickhouse, N. S., Kashyap, V., Laming, J. M., Huenemoerder, D. P., Smith, R., & Wargelin, B. J. 2001, ApJ, 548, L81
Drake, J. J., & Testa, P. 2005, Nature, 436, 525
Drake, J. J., Testa, P., & Hartmann, L. 2005, ApJ, 627, L149
Drew, J. E., Busfield, G., Hoare, M. G., Murdoch, K. A., Nixon, C. A., & Oudmaijer, R. D. 1997, MNRAS, 286, 538
Dullemond, C. P., & Dominik, C. 2004, A&A, 421, 1075
Esteban, C., Peimbert, M., García-Rojas, J., Ruiz, M. T., Peimbert, A., & Rodríguez, M. 2004, MNRAS, 355, 229
Feigelson, E. D., Broos, P., Gaffney, J. A., III, Garmire, G., Hillenbrand, L. A., Pravdo, S. H., Townsley, L., & Tsuboi, Y. 2002, ApJ, 574, 258
Franciosini, E., Scelsi, L., Pallavicini, R., & Audard, M. 2007, A&A, 471, 951
Fruscione, A., et al. 2006, Proc. SPIE, 62701V
Güdel, M., Audard, M., Reale, F., Skinner, S. L., & Linsky, J. L. 2004, A&A, 416, 713
Gabriel, A. H., & Jordan, C. 1969, MNRAS, 145, 241
Gabriel, A. H., & Jordan, C. 1973, ApJ, 186, 327
Gagne, M., & Caillault, J.-P. 1994, ApJ, 437, 361
Gagné, M., Oksala, M. E., Cohen, D. H., Tonnesen, S. K., ud-Doula, A., Owocki, S. P., Townsend, R. H. D., & MacFarlane, J. J. 2005, ApJ, 628, 986
García-Alvarez, D., Drake, J. J., Lin, L., Kashyap, V. L., & Ball, B. 2005, ApJ, 621, 1009
Getman, K. V., et al. 2005, ApJS, 160, 319
Gondoin, P. 2005, A&A, 444, 531
Grady, C. A., Woodgate, B., Bruhweiler, F. C., Boggess, A., Plait, P., Lindler, D. J., Clampin, M., & Kalas, P. 1999, ApJ, 523, L151
Grady, C. A., et al. 2004, ApJ, 608, 809
Grady, C. A., et al. 2005, ApJ, 630, 958
Gu, M. F., Gupta, R., Peterson, J. R., Sako, M., & Kahn, S. M. 2006, ApJ, 649, 979
Guimarães, M. M., Alencar, S. H. P., Corradi, W. J. B., & Vieira, S. L. A. 2006, A&A, 457, 581
Hamaguchi, K., Yamauchi, S., & Koyama, K. 2005, ApJ, 618, 360
Herbig, G. H. 1960, ApJS, 4, 337
Herbig, G. H., & Griffin, R. F. 2006, AJ, 132, 1763
Houck, J. C., & Denicola, L. A. 2000, in ASP Conf. Ser. 216, Astronomical Data Analysis Software and Systems IX, ed. N. Manset, C. Veillet, & D. Crabtree (San Francisco, CA: ASP), 591
Huenemoerder, D. P., Canizares, C. R., & Schulz, N. S. 2001, ApJ, 559, 1135
Huenemoerder, D. P., Kastner, J. H., Testa, P., Schulz, N. S., & Weintraub, D. A. 2007, ApJ, 671, 592
Hummel, C. A., Armstrong, J. T., Quirrenbach, A., Buscher, D. F., Mozurkewich, D., Elias, II, N. M., & Wilson, R. E. 1994, AJ, 107, 1859
Ishibashi, K., Dewey, D., Huenemoerder, D. P., & Testa, P. 2006, ApJ, 644, L117
Ku, W. H.-M., Righini-Cohen, G., & Simon, M. 1982, Science, 215, 61
Liefke, C., Ness, J., Schmitt, J. H. M. M., & Maggio, A. 2008, A&A, 491, 895
Maggio, A., Flaccomio, E., Favata, F., Micela, G., Sciortino, S., Feigelson, E. D., & Getman, K. V. 2007, ApJ, 660, 1462
Mannings, V., & Sargent, A. I. 1997, ApJ, 490, 792
Mazzotta, P., Mazzitelli, G., Colafrancesco, S., & Vittorio, N. 1998, A&AS, 133, 403
Muzerolle, J., D'Alessio, P., Calvet, N., & Hartmann, L. 2004, ApJ, 617, 406
Ness, J., Brickhouse, N. S., Drake, J. J., & Huenemoerder, D. P. 2003, ApJ, 598, 1277
Palla, F., & Stahler, S. W. 1993, ApJ, 418, 414
Parenago, P. P. 1954, Trudy Gosudarstvennogo Astronomicheskogo Instituta, 25, 1
Pizzolato, N., Maggio, A., Micela, G., Sciortino, S., & Ventura, P. 2003, A&A, 397, 147
Preibisch, T., Balega, Y., Hofmann, K.-H., Weigelt, G., & Zinnecker, H. 1999, New Astron., 4, 531
Prosser, C. F., Randich, S., Stauffer, J. R., Schmitt, J. H. M. M., & Simon, T. 1996, AJ, 112, 1570

Reale, F. 2007, A&A, 471, 271
Robrade, J., & Schmitt, J. H. M. M. 2006, A&A, 449, 737
Schaller, G., Schaerer, D., Meynet, G., & Maeder, A. 1992, A&AS, 96, 269
Schröder, C., & Schmitt, J. H. M. M. 2007, A&A, 475, 677
Schulz, N. S., Canizares, C., Huenemoerder, D., Kastner, J. H., Taylor, S. C., & Bergstrom, E. J. 2001, ApJ, 549, 441
Schulz, N. S., Canizares, C., Huenemoerder, D., & Tibbets, K. 2003, ApJ, 595, 365
Schulz, N. S., Testa, P., Huenemoerder, D. P., Ishibashi, K., & Canizares, C. R. 2006, ApJ, 653, 636
Siess, L., Dufour, E., & Forestini, M. 2000, A&A, 358, 593
Smith, R. K., Brickhouse, N. S., Liedahl, D. A., & Raymond, J. C. 2001, ApJ, 556, L91
Stelzer, B., Flaccomio, E., Montmerle, T., Micela, G., Sciortino, S., Favata, F., Preibisch, T., & Feigelson, E. D. 2005, ApJS, 160, 557
Stelzer, B., Huélamo, N., Micela, G., & Hubrig, S. 2006a, A&A, 452, 1001
Stelzer, B., Micela, G., Hamaguchi, K., & Schmitt, J. H. M. M. 2006b, A&A, 457, 223
Telleschi, A., Güdel, M., Briggs, K. R., Skinner, S. L., Audard, M., & Franciosini, E. 2007, A&A, 468, 541
Testa, P., Drake, J. J., & Peres, G. 2004, ApJ, 617, 508
Testa, P., Huenemoerder, D. P., Schulz, N. S., & Ishibashi, K. 2008, ApJ, 687, 579
Testa, P., Reale, F., Garcia-Alvarez, D., & Huenemoerder, D. P. 2007, ApJ, 663, 1232
Vilhu, O., & Rucinski, S. M. 1983, A&A, 127, 5
Vink, J. S., Drew, J. E., Harries, T. J., Oudmaijer, R. D., & Unruh, Y. 2005, MNRAS, 359, 1049
Walter, F. M., & Bowyer, S. 1981, ApJ, 245, 671
Waters, L. B. F. M., & Waelkens, C. 1998, ARA&A, 36, 233
Wood, B. E., Redfield, S., Linsky, J. L., Müller, H.-R., & Zank, G. P. 2005, ApJS, 159, 118
Zinnecker, H., & Preibisch, T. 1994, A&A, 292, 152